DETECTION OF LANDSLIDES IN THE 2015 GORKHA, NEPAL EARTHQUAKE USING SATELLITE IMAGERY

Risako Tsuchida[1], Wen Liu[1] and Fumio Yamazaki[1]
[1]Chiba University, 1-33 Yayoi-cho, Inage-ku, Chiba 63-8522, Japan,
Email: aema0123@chiba-u.jp; wen.liu@chiba-u.jp; fumio.yamazaki@faculty.chiba-u.jp

ABSTRACT: On April 25, 2015, an Mw7.8 earthquake struck the Gorkha district of Nepal. This earthquake caused serious damages to roads and rivers due to many landslides and avalanches. Particularly, numerous collapses of slopes occurred in the middle altitude zone of the northern Nepal due to mainly by the mainshock and some by aftershocks. Therefore the purpose of this study is to extract the landslides caused by the earthquake using satellite images. The pre- and post-event ALOS-2 PALSAR-2 images and Landsat 8 optical images were used in this purpose. PALSAR-2 is an active L-band microwave sensor to achieve cloud-free day-and-nighttime observation, so it is an extremely important source for early damage assessment when a disaster occurs in inaccessible mountain areas. We clarified the specific characteristics of landslide areas and performed an automated extraction method. Furthermore, the results were evaluated by comparing with that by visual interpretation of the optical images. By this comparison, large-scale landslides were extracted well from the PALSAR-2 images.

1. INTRODUCTION

An Mw7.8 earthquake jolted Gorkha district, Nepal at 11:56 am (local time) on April 25, 2015. The epicenter was located 28.147° N, 84.708° E, with a depth of 15 km. This earthquake caused significant damages, in particular, to buildings, infrastructures and road networks. Since the focal zone was located in the mountain area, and thus many landslides and avalanches were generated and they interrupted roads and rivers. Then many villages were isolated and the property and living of inhabitants were threatened. Although information gathering at an early stage is quite important for emergency response, the access to the affected zones from the ground was difficult, especially to the mountainous areas.

In such a case, remote sensing from satellites and airplanes is a powerful alternative. Optical sensors can provide information on the ground surface that anyone understands, but cannot observe under a cloud-over condition or at nighttime. Synthetic aperture radar (SAR) is free from these restrictions and thus becomes more conveniently used, especially in post-disaster response (Yamazaki and Matsuoka, 2007; Rathje and Adams, 2008). The extraction of damaged buildings due to earthquakes (Dell'Acqua and Gamba, 2012) and inundated areas due to floods and tsunamis (Liu et al., 2013) has been carried out by a number of researchers using SAR intensity data.

The extraction of landslides using satellite SAR images and the optical sensor is carried out frequently all over the world (Yamazaki et al., 2011). However, there are still few studies to evaluate the accuracy of landslide extraction and to analyze SAR intensity images of ALOS-2 PALSAR-2 for mountainous areas. ALOS-2 (also called "Daichi-2" in Japanese) with an enhanced synthetic aperture radar (SAR) PALSAR-2 sensor is the only one L-band SAR satellite in the world, succeeding its predecessor, ALOS PALSAR.

In this study, we examine the SAR backscattering characteristics of landslide areas using PALSAR-2 images acquired at pre- and post-event times, and attempt an automated extraction method. Compared with pre- and post-event Landsat 8 images, the accuracy of the landslide extraction from the L-band SAR is evaluated.
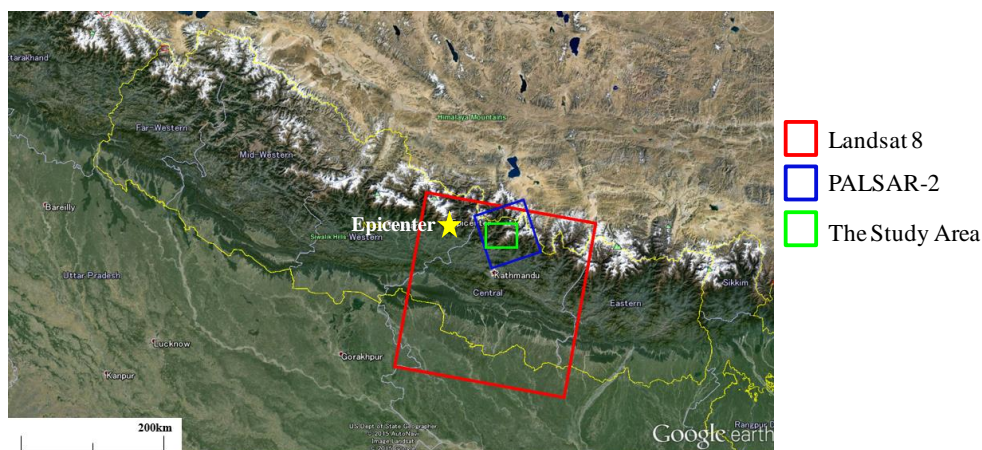
2. THE STUDY AREA AND IMAGE DATA

This study focuses on the valleys along the Trishuli river and the Langtang river. The region is located in the Nepali Himalayas bordering Tibet to the north of the Kathmandu Valley, shown in **Figure 1**. After the earthquake, widespread landslides, rock falls and avalanches were reported in this region. The landslides affected river flows and caused significant impacts to the villages in these valleys (National Aeronautics and Space Administration, 2015; International Charter, 2015).

The pre- and post-event PALSAR-2 images were used to detect geological hazards in the target area. The pre-event PALSAR-2 image was taken on February 11, 2015 whereas the post-event one on May 2, 2015, one week after the

mainshock. These images were captured with the HH and HV polarizations in the StripMap mode. The resolution of the images was 5.0 m with the off-nadir angle 32.5 degrees. The images were acquired from the ascending path with the right look.

The pre-event Landsat 8 image taken on February 9, 2015 and the post-event one on June 1, 2015 (**Figure 1**) were also used to detect landslide from the optical images. The both images were taken from the path no. 141 and row no. 41. In addition, ASTER GDEM (resolution 30m) was employed to grasp the topography of the target area. To select this study area, the preliminary landslide inventory map (British Geological Survey, 2015) was mainly used.

(a) The study area and the satellite images



(b) Pre-event Landsat 8

(c) Post-event Landsat 8

Figure 1 The study area in the central Nepal and the coverage of the satellite images used (**a**),
and the pre-event (**b**) and the post-event Landsat 8 images for the study area (**c**)

3. THE METHOD OF LANDSLIDE EXTRACTION

The flowchart of this study is shown in **Figure 2**. First, the areas of landslides were extracted from the Landsat-8 images. In the preprocessing step, the digital numbers (DNs) were converted into the Top-Of-Atmosphere (TOA) reflectance. Then, in order to enhance the spatial resolution, a pan-sharpening procedure was applied to the multispectral bands (30-m resolution) using the panchromatic band (15-m resolution). First, visual inspection of landslides was carried out. For vegetated mountainous areas, landslides often remove the existing vegetation and bare lands are exposed. Thus the Normalized Difference Vegetation Index (NDVI) was calculated for the pre- and post-event Landsat 8 images to extract pixels where the NVDI values were decreased due to landslides (Miura and Midorikawa, 2008; Liu and Yamazaki, 2008). The introducing the digital elevation model (DEM), the characteristics of landslides with respect to the slope angle was investigated following the previous work (Ishide and Yamazaki, 2010). Supervised classification was also applied to extract landslides using the post-event Landsat 8 image.

The extraction of landslides was also attempted using the PALSAR-2 data. The original DN values of the PALSAR-2 intensity data were converted to the backscattering coefficients (sigma naught: σ_0), the radar reflectivity in the unit area. After this conversion, all the backscattering coefficients (HH and HV) of the two SAR images were

in the range between -30 dB and 30 dB. Then, an Enhanced Lee filter (Lopes et al., 1990) was applied with the window size of 5 × 5 pixels, in order to reduce the speckle noise. The backscattering coefficients in the landslide areas (from the optical images) were extracted and their characteristics were investigated. Finally, all the results of the landslide extractions were compared and the accuracy was discussed
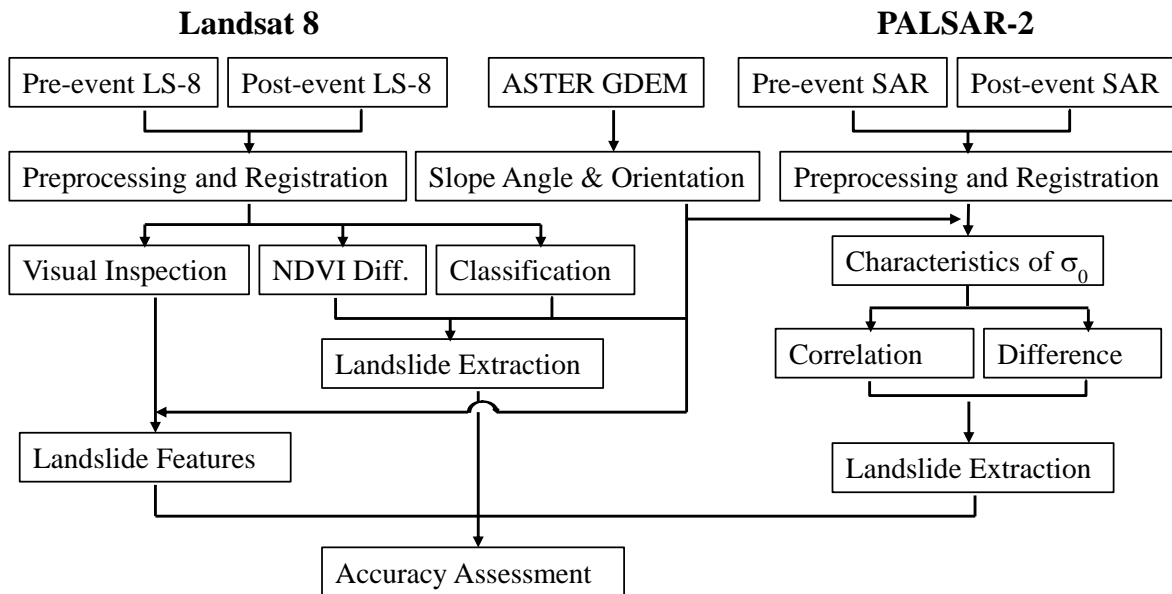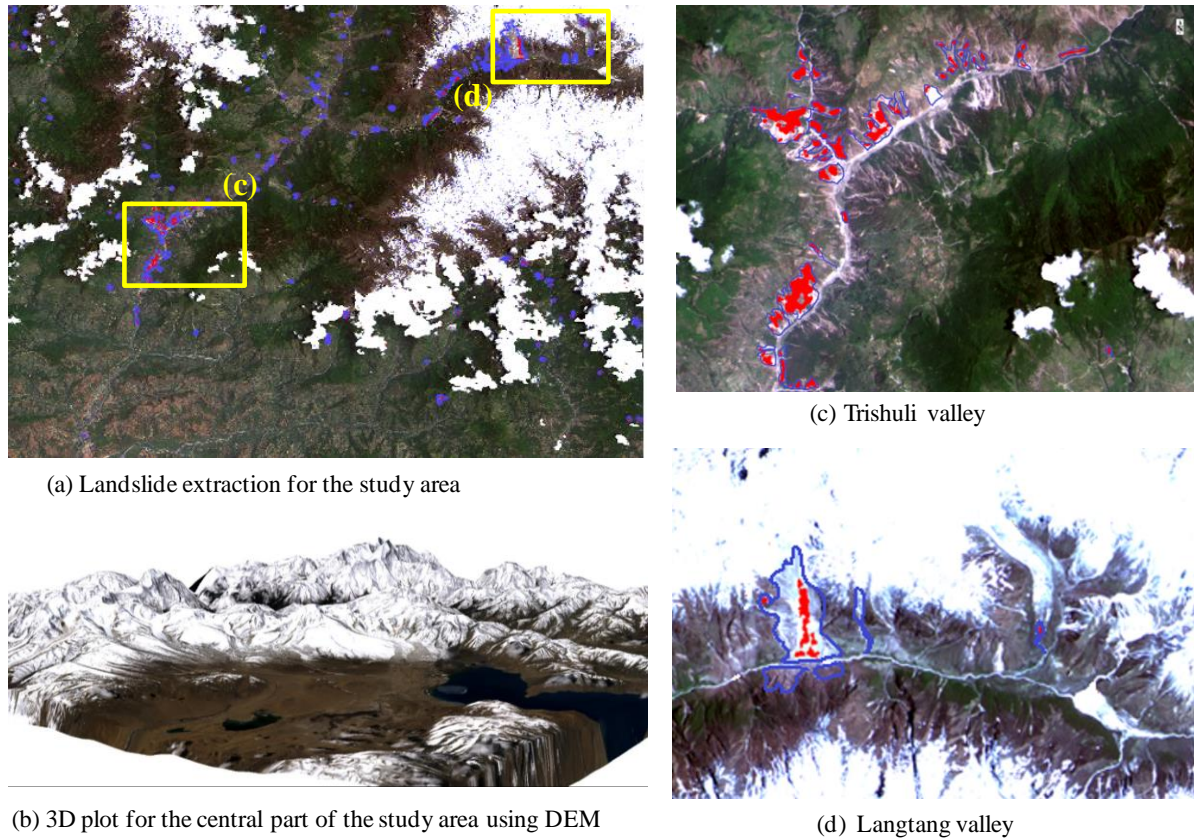
Figure 2 The flowchart of this study

4. EXTRACTION OF LANDSLIDES FROM LANDSAT-8 IMAGES

4.1 Extraction of landslides using NDVI

The study area was mostly covered by vegetation and some by snow (ice) in the high altitude zone. Thus, we assumed first that landslides cause the reduction of NDVI values due to exposure of bare soil. Since the pre-event image was taken in winter (February) and the post-event one in early summer (June), the NDVI was supposed to increase in the most pixels. If the NDVI was decreased, landslides might be occurred in the corresponding area. Thus we assumed that the pixels with reduced NDVI vales after the earthquake as landslide areas. Since some clouds existed in the post-event image and they caused false alarms, these areas were removed manually.

In this ways, 502,658 pixels were extracted as landslides in the study area. **Figure 3** shows the post-event Landsat 8 image with the results of our visual inspection (blue line) and that from reduced NDVI values (red pixels). From this comparison, the extracted pixels are generally seen to agree well with the actual landslides. A three-dimensional plot of the pre-event Landsat 8 image superposing on the ASTER GDEM is shown in **Figure 3 (b)**. Form the plot, it is clearly observed that the study area is surrounded by snow-covered high mountains and rivers go down through the valleys

In order to observe more in detail, two areas with many landslides were selected. **Figure 3(c)** shows the area along the Trishuli river valley. In this area, landslides were extracted well by the NDVI difference for the places where vegetation was changed to bare soil. But it was not successful for the pixels where the surface was bare soil before the earthquake. For the Langtang river valley shown in **Figure 3(d)**, only the slope failures that occurred in the low altitude zone were extracted properly by the reduction of NDVI values. We could not detect other failures of ice/snow covered slopes in the high altitude zone.

(a) Landslide extraction for the study area

(c) Trishuli valley

(b) 3D plot for the central part of the study area using DEM

(d) Langtang valley

Figure 3 The post-event Landsat-8 image with the results of visual inspection (blue line) and from reduced NDVI values (red pixels) for the whole study area **(a)**, the Trishuli valley **(c)**, and the Langtang valley **(d)**. 3D plot of the pre-event Landsat 8 image using ASTER DEM is shown in **(b)**.

4.2 Correction of the extraction results using DEM

The landslides and slope failures are related to the slope angle as well as other parameters of the slope, such as surface geology, vegetation, water content etc. Using the DEM, the slope angles were calculated for the study area. We compared the slope with the visual observation, and checked each other's relations. **Figure 4** shows the histogram of pixels with or without landslide by visual inspection in terms of slope angle. The occurrence ratio of landslide (green line for each 10 degrees interval) is seen to increase until the slope angle reach 50 degrees. The ratio goes down for the slopes steeper than 50 degrees, but this is probably due to snow/ice cover and also rocky surfaces.

The ratio is negligible for pixels less than 5 degrees, but in the range of 5 to 10 degrees, the ratio has a meaningful ratio (0.96 %). We examined the slope failures with small slope angles and found that they were mostly a part of large failures. Similar situation was observed from ALOS AVNIR-2 optical satellite images in the 2008 Sichuan, China earthquake (Liu and Yamazaki, 2008). Thus following the previous study by Ishide and Yamazaki (2010), we assumed that landslides do not occur in the area with less than 10 degrees, and removed from the detection result. The number of extracted pixels became 485,910 after this filter, and some errors in flatland were removed.

Table 1 shows the extraction results based on the landslide area, estimated from visual inspection In this table, the rate of detection shows a big difference at the size of landslide 675 m^2 (the area for three pan-sharpened pixels for Landsat 8) or larger. Since the size of the original multispectral-band's pixel is 900 m^2, the limitation due to the spatial resolution exists, both for visual inspection and image processing approach. If a landslide shares the area larger than three pan-sharpened pixels, about 90% of them were extracted at least to some parts by the NDVI difference. The other causes of false negative errors were the low contrast of the pre-event image, and thus even visual inspection might include some errors. To avoid such errors, high-resolution optical images should be introduced in a future study.
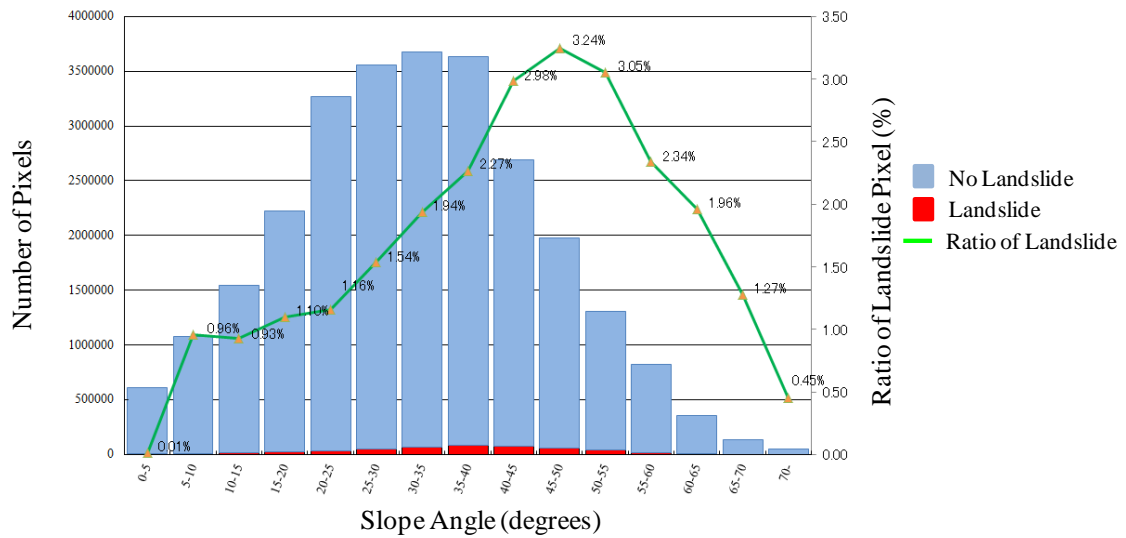
Figure 4 Histograms of Landsat-8 pixels with or without landslide in terms of the slope angle

Table 1 The number of extracted landslide locations based on visual inspection, the difference of NDVI values, and the classification of the post-event Landsat-8 image

| Landslide Area	Visual inspection	From NDVI	Classification of post-event LS-8 image
Smaller than 675 m^2	254	119 (46.9%)	121 (47.6%)
Larger than 675 m^2	318	284 (89.3%)	295 (92.8%)
Total	572	403 (70.5%)	416 (72.7%)

4.3 Extraction of landslides based on supervised classification

When the landslides occur, soil is often exposed. We can find landslide-affected areas easily by comparing the pre- and post-event optical images. Thus, maximum likelihood supervised classification was carried out for the pre- and post- event Landsat-8 images, and tried to extract pixels which have changed to soil surface after the earthquake. Two methods were attempted for the supervised classification to extract landslides. The first method classified the pre- and post-event images separately and extracted the pixels changed to soil from other land-covers. But some difficulties were found in this approach. Since there was a difference in the season, the extent of snow/ice was very different as well as the activity of vegetation. Hence if snow melted and soil came out, such pixels were recognized as landslides. Thus the post-event soil areas should be further classified into three types: original soil, snow-melted soil, and landslide soil.

Due to this reason, we decided to use only the post-event Landsat-8 image to extract landslide pixels. For the study area shown in **Figure 1**, supervised classification by the maximum likelihood method was carried out using the 7 optical and short-wave infrared bands of the Landsat-8 pan-sharpened multispectral images, as shown in **Figure 5(a)**. In the classification, training areas for six classes were assigned such as landslide soil, non-landslide soil, vegetation, ice and snow, cloud, and river water. Landslide soil was seen to have a slightly different color than non-landslide soil. But for some areas, the difference was very subtle, and thus the pre-event image was referred to assign the training areas of these two types of soil.

After the supervised classification, the pixels with the slope angle less than 10 degrees were removed from the results to reduce the miss-classification (false positive). As the result, the number of the pixels which were classified as landslides was 533,679. **Figure 5 (b)** shows the enlarged result along the Trishuli valley. Compared with **Figure 3 (c)**, the extracted landslides along the valley are seen to agree well with the results by the manual extraction and from the NDVI difference.

Table 2 compares the extraction accuracy of the two extraction methods at the pixel unit of landslides for the study area. The producer accuracy is the ratio of the extracted pixels out of the truth data of the concerned land-cover class (landslide). On the contrary, the user accuracy is the ratio of correctly extracted pixels out of all the extracted pixels of the concerned land-cover class. The supervised classification using only the post-event Landsat-8 image showed better results for both the producer and user accuracies. But this conclusion is not a general one applicable to other cases. In some cases, landslide soil and none-landslide soil may be difficult to distinguish even visually. Pre-existing bare soil may be misjudged as landslides. Thus the pre-event image is still very useful to grasp the pre-event condition and to extract changes caused by natural disasters.

(a) The study area

(b) Trishuli valley

Landslide
Soil
Vegetation
Snow
Cloud
Unclassified
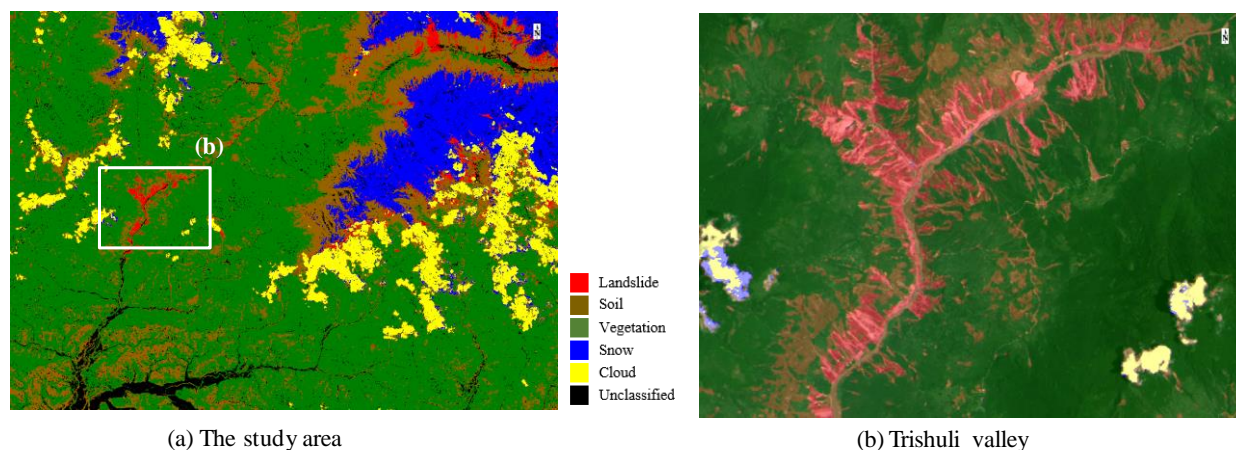
Figure 5 The result of supervised classification using only the post-event Landsat-8 image for the study area **(a)** and for the Trishuli valley **(b)**

Table 2 Extraction accuracy of landslides by area (pixels) from Landsat 8 images for the study area

Extraction Accuracy	From NDVI's Difference	Supervised classification
Producer Accuracy	72.10 %	76.30 %
User Accuracy	75.50 %	82.70 %

: Image Analysis
: Visual Inspection
Producer Accuracy: B/(B+C)
User Accuracy: B/(A+B)

5. EXTRACTION OF LANDSLIDES FROM PALSAR-2 IMAGES

5.1 Characteristic of the backscattering coefficient in the SAR images

Due to side-looking viewing geometry of SAR, acquired SAR intensity images are highly affected by the incidence angle of radar to the earth surface and its 3D configuration. Layover, foreshortening, radar shadow are typical topographic effects that SAR intensity data are suffered from. These topographic effects are very strong in the mountainous regions, like the study area of this paper. Hence, it is necessary to examine the observation condition carefully depending on the locations because the slope angle and the orientation of the slope with respect to the radar illumination were different.
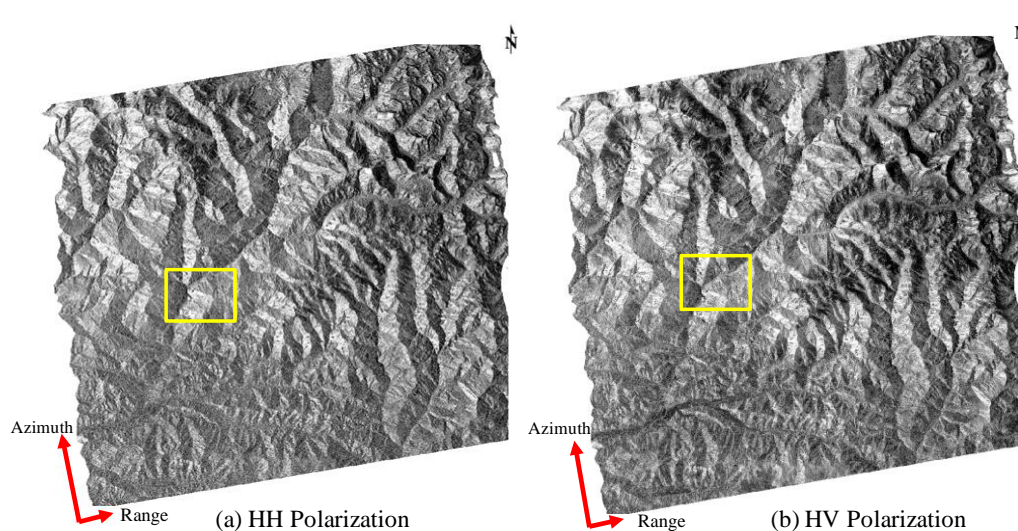
Figure 6 shows the backscattering coefficient of the post-event PALSAR-2 image for the HH and HV polarizations. The sigma naught values for the HH polarization were generally bigger (brighter) than those for the HV polarization. They look very similar, but the contrast in the image is clearer for the HV polarization. It is considered that the multiple and volume scattering characteristics of vegetation and snow greatly influenced this observation although the L-band microwave is generally considered to penetrate vegetation. The pre-event PALSAR-2 image is very similar with the post-event one in this small scale, and thus not shown here.

In order to observe more details of the SAR images of the dual polarizations, the color composites of the pre- and post-event PALSAR-2 σ_0 images are depicted in **Figure 7** for the Trishuli valley area. In the color composite, red
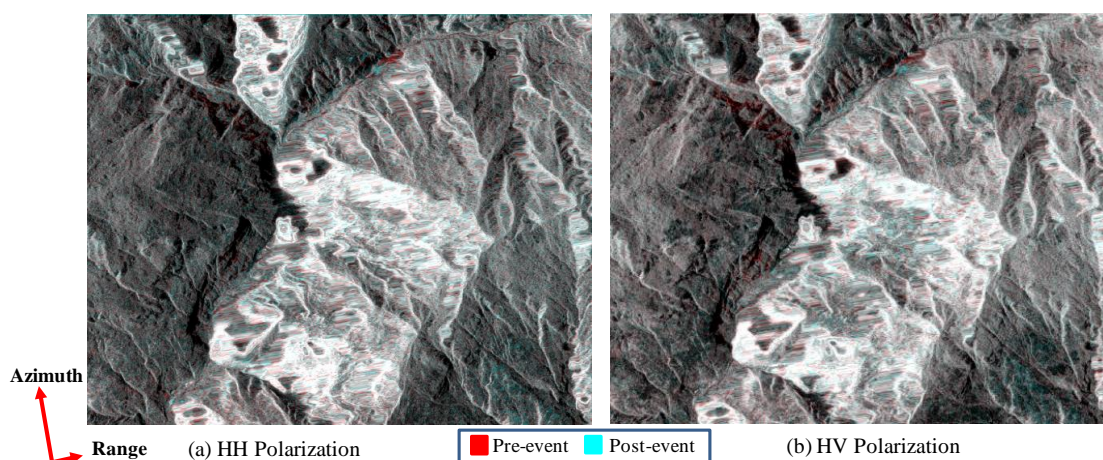
color was assigned for the pre-event image while cyan (blue + green) color for the post-event one. Thus the areas with gray scale colors show no change between the two time instants, those with red with decreased backscatter, those with cyan increased backscatter after the earthquake. Both red- and cyan-colored areas are recognized along the river valley, which might be caused by landslides. But the most parts of the image is in gray colors from dark zones, e.g. rivers and radar shadows, to very bright zones, e.g. mountain slopes facing to the radar illumination. Thus the topographic condition was seen to be the dominant factor to determine SAR backscatter in mountainous areas, like this study area.

Figure 8 shows the distribution of the backscattering coefficients (the post-event image for the study area) with respect to the slope orientation, clockwise from the north. Since the SAR images were acquired from the ascending path, the microwave was illuminated from the west (84.3 degrees from the north). Thus many pixels of high σ_0 values are observed for areas with slope-orientation about 264.3 degrees while low values for areas with slope-orientation about 84.3 degrees. Based on this result, the slopes with the orientation range from 235 degrees to 295 degrees were extracted as a similar slope-orientation group with respect to the radar illumination.
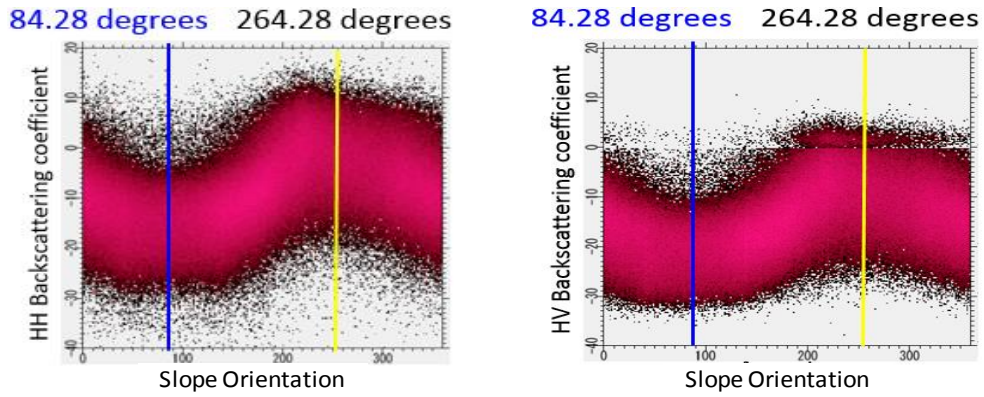
Figure 9 plots the relationship between the backscattering coefficients (for the selected slope-orientation group) and the slope angle (gradient). Since the off-nadir angle of the radar incidence was 32.5 degrees, the backscatter shows the highest values around the slope angle of 32.5 degrees. From these observations, the slope orientation and angle were found to be important factors to determine SAR backscatter, more than the surface materials and conditions.

Azimuth

Range (a) HH Polarization

Azimuth

Range (b) HV Polarization

Figure 6 PALSAR-2 backscattering coefficient (σ_0) images acquired on May 2, 2015

Azimuth

Range (a) HH Polarization

Pre-event Post-event (b) HV Polarization

Figure 7 Color composite of the pre- and post-event PALSAR-2 σ_0 images for the Trishuli valley

84.28 degrees 264.28 degrees   84.28 degrees 264.28 degrees

(a) HH polarization   (b) HV polarization

Figure 8 Relationship between the backscattering coefficients and slope orientation

32.5 degrees   32.5 degrees
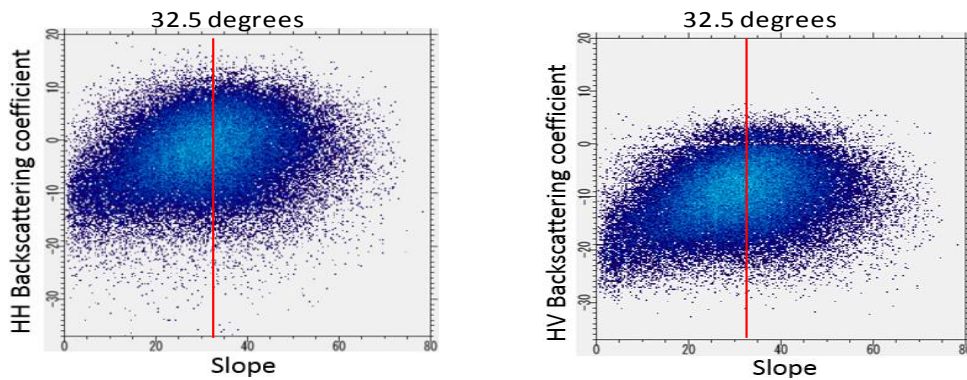
(a) HH polarization   (b) HV polarization

Figure 9 Relationship between the backscattering coefficients and slope angle
(for slop-orientation in the range from 235 to 295 degrees)

5.2 Extraction of landslide areas from SAR images

In order to extract the changes due to the earthquake, the correlation coefficient and the between the pre- and post-event SAR images were calculated for the HH and HV polarization in the Trishuli valley. The window size was set as 15 × 15 pixels after a few trials. In **Figure 10**, the reduction of the correlation coefficient was observed in both the HH and HV polarizations. But the reduced correlation includes the seasonal changes, such as those of vegetation and snow. The difference between the pre- and post-event images, shown in **Figure 11**, is seen to have more positive areas in the HV polarization, probably due to the increased vegetation in the post-event time (May).
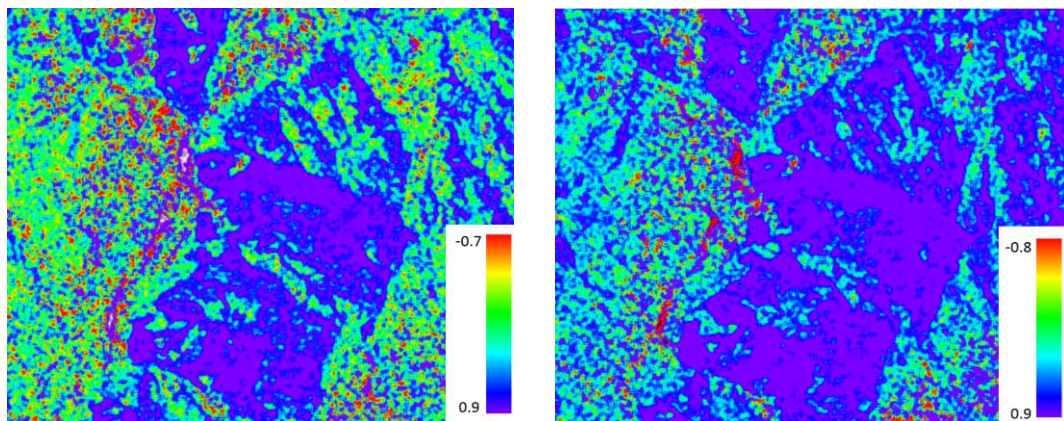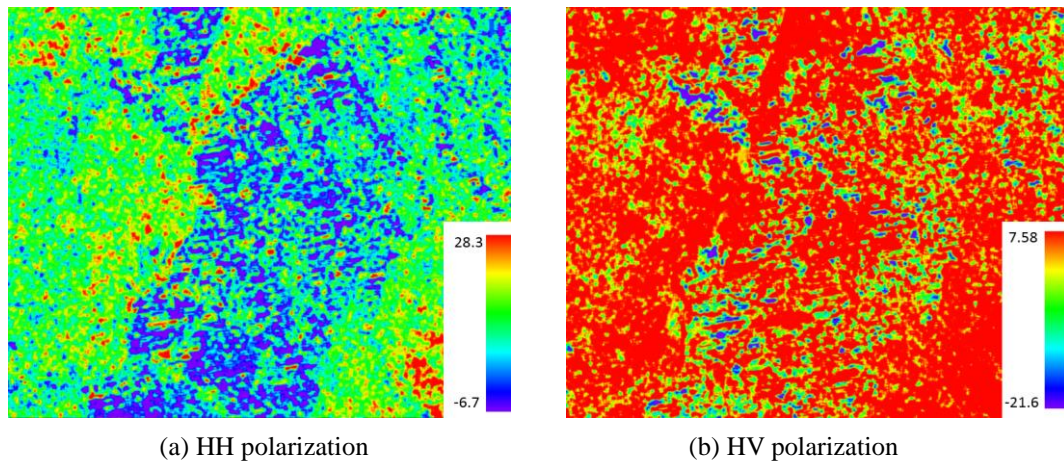

(a) HH polarization   (b) HV polarization

Figure 10 The correlation coefficient between the pre- and post-event σ_0 values in the Trishuli valley
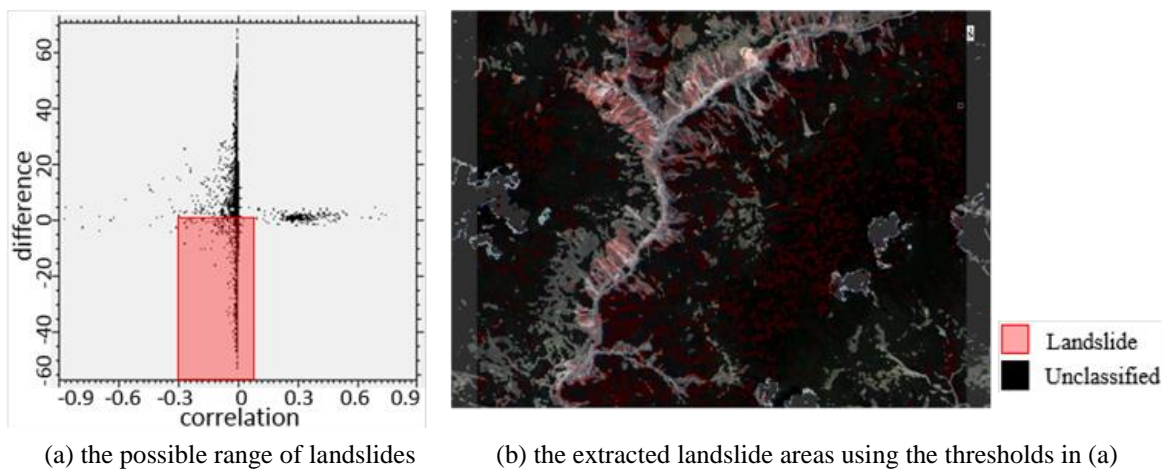
(a) HH polarization (b) HV polarization

Figure 11 The difference between the pre- and post-event σ_0 values in the Trishuli valley

In order to examine the characteristics of σ_0 values in landslide areas, **Figure 12 (a)** plots the relationship between the correlation coefficient and the difference for the Trishuli valley area. In this result, at the locations where landslides occurred, the correlation coefficient was in the range from -0.3 to 0.1, and the difference in the range less than 0, by visual inspection comparing with the optical images. In order to examine only the possible landslides, the post-event Landsat-8 classification results corresponding to vegetation and snow classes were masked as shown in **Figure 12 (b)**. After this manipulation, the extracted areas by the thresholding of the two indices agree reasonably well with the extracted results from the classification of the post-event Landsat-8 image.

In case of SAR images for mountainous regions, the backscatter is highly affected by the orientation and angle of slopes, more than surface materials and conditions. Furthermore, the situation of snow and vegetation were dependent on the altitude in this example. Thus it was difficult to extract landslides using only the parameters from the SAR images even the pre- and post-event images in the same observation conditions were available. Thus, the inspection on a case-by-case basis was necessary together with other available data.

(a) the possible range of landslides (b) the extracted landslide areas using the thresholds in (a)

Figure 12 The possible range of landslides in the correlation coefficient vs. difference plot (a) and the extracted landslide areas after masking. These results were for the HH polarization.

6. CONCLUSIONS

The 2015 Gorkha, Nepal earthquake occurred in the mountainous region, and thus many landslides and avalanches were triggered and them blocked rivers and roads. In this study, the extraction of landslides was attempted using pre- and post-event Landsat-8 and PAlSAR-2 imagery data. The region including the valleys along Trishuli and Langtang rivers was selected as the study area since many landslides were reported there. Using the pre- and post-event Landsat-8 images, visual inspection of landslides was carried out first. Employing ASTER GDEM, landslides were found to occur with a higher probability as the slope angle gets steeper.

The difference of the NDVI values between the two time instants was used first to extract landslides since vegetation was removed and bare soil was exposed after a landslide, causing the reduction of NDVI. The supervised classification of the post-event Landsat-8 image was also carried out to distinguish landslide and none-landslide soils. By these methods, landslides larger than three pixels of the optical image were extracted with a high probability. The classification method using only the post-event optical image gave better user and producer accuracies, both about 80 % in the landslide pixels extraction. Since the seasonal changes were included between the two-temporal images, especially in vegetation and snow, classification using the two images was less accurate.

Using the pre- and post-event PALSAR-2 images, the characteristics of the backscattering coefficient were investigated first with respect to the orientation and angle of mountain slopes. The result showed that the backscatter was more affected by these topographical parameters than the land-cover conditions in the mountainous region. Hence the correlation coefficient and the difference between the pre- and post-event SAR data were examined only for a selected topographic condition. Introducing the classification result from the optical images, the landslide pixels were characterized by these two indices. The use of satellite SAR images is promising as a tool of information gathering after the occurrence of natural disasters. We will continue a further research on landslide extraction for the Nepal earthquake and other events in order to establish a more reliable and versatile method.

ACKNOWLEDGMENTS

REFERENCE

British Geological Survey, Nepal earthquake response 2015, 2015, from
    http://www.bgs.ac.uk/research/earthHazards/epom/nepalEarthquakeResponse.html.
Dell'Acqua, F., & Gamba, P. 2012. Remote sensing and earthquake damage assessment experiences, limits, and perspectives, Proceedings of the IEEE, 100, pp. 2876–2890.
International Charter - Space and Major Disasters, 2015, Earthquake and landslide in Nepal and India, from
    https://www.disasterscharter.org/web/guest/activations/charter-activations
Ishide, T., Yamazaki, F., 2010. Detection of slope failures using ALOS/AVNIR-2 images for the 2008 Iwate-Miyagi Inland Earthquake. Journal of Japan Association for Earthquake Engineering, 10(3), pp. 12-24 (in Japanese).
Japan Aerospace Exploration Agency, ALOS-2/PALSAR-2 Observation Results of the 2015 Nepal Earthquake, 2015, from http://www.eorc.jaxa.jp/ALOS-2/en/img_up/dis_pal2_npl-eq_20150426_2.htm
Liu, W., Yamazaki, F., 2008. Damage Detection of the 2008 Sichuan, China Earthquake from ALOS optical images. 28th Asian Conference on Remote Sensing, Paper No. 119, CD-ROM, 6p.
Liu, W., Yamazaki, F., Gokon, H. & Koshimura, S. 2013. Extraction of tsunami-flooded areas and damaged buildings in the 2011 Tohoku-Oki Earthquake from TerraSAR-X intensity images, Earthquake Spectra, 29(S1). S183-S200.
Lopes, A., Touzi, R., Nezry, E., 1990. Adaptive speckle filters and scene heterogeneity. IEEE, Trans Geosci Remote Sens 28(6), pp. 992–1000.
Miura, H. and Midorikawa, S., 2008. Detection of Slope Failure Areas Using High-Resolution Satellite Images and Digital Elevation Model for the 2004 Niigata-Ken Chuetsu, Japan Earthquake. Proceedings of 5th International Conference on Urban Earthquake Engineering, pp.559-564.
National Aeronautics and Space Administration (NASA),Generated Damage Map to Assist with 2015 Gorkha, Nepal Earthquake disaster response, 2015, from
    https://www.nasa.gov/jpl/nasa-generated-damage-map-to-assist-with-2015-gorkha-nepal-earthquake-disaster.
Rathje, E., and Adams, B.J. 2008. The role of remote sensing in earthquake science and engineering, Opportunities and Challenges, Earthquake Spectra, 24(2), pp. 471–492.
Yamazaki, F., Matsuoka, M., 2007. Remote sensing technologies in post-disaster damage assessment, Journal of Earthquake and Tsunami, 1(3), pp. 193-210.
Yamazaki, F., Inoue, H., Liu, W., 2011. Characteristics of SAR backscattered intensity and its application to earthquake damage detection. Computational Stochastic Mechanics, Edited by G. Deodatis and P. D. Spanos, Research Publishing, ISBN: 978-981-08-7619-7, pp. 602-606.